The Underlying Event at the LHC

D. Acosta[a], F. Ambroglini[b], P. Bartalini[a], A. De Roeck[c], L. Fanò[b], R. Field[a], K. Kotov[a]

a: University of Florida, FL, USA

b: Perugia University and INFN, Perugia, Italy

c: CERN, Geneva, Switzerland

Abstract

We discuss a study of "minimum bias" collisions and the "underlying event" at CMS (under nominal conditions) by measuring charged particles and muons. The underlying event is studied by examining charged particles in the "transverse" region in charged particle jet production and in the "central" region of Drell-Yan muon-pair production (after removing the muon-pair).

1   Introduction

In order to find "new" physics at a hadron-hadron collider it is essential to understand the features of the "ordinary" QCD processes. One must not only consider the hard scattering part of the process, but also the underlying event (UE), *i.e.*, the softer component of the collision accompanying the hard scattering which accounts for a large fraction of the activity in terms of multiplicity and momentum of the observed particles.

This note describes the UE measurement plan and measurement strategy in nominal CMS conditions at low luminosity. The document is sub-divided in six sections and one appendix. The next section gives the definition of the studied processes. A brief review of the current status of the phenomenological studies and theoretical models is given in section 3. The measurement plan at the LHC is described in section 4, where the relevant observables sensitive to the examined processes are introduced by comparing different tunings of the most popular Monte Carlo models. The feasibility study of the UE measurement in jet and Drell-Yan events for nominal CMS conditions at low luminosity is reported in section 5. The conclusions of this study are briefly discussed in section 6. The envisaged measurements rely on the optimization of soft track reconstruction in nominal CMS conditions. Details of the performances of the CMS track reconstruction algorithm optimized for this study are reported in Appendix A.

2   Definition of the physics process

Events collected with a trigger that is not very restrictive are referred to as minimum bias events (MB). The total proton-proton cross section is the sum of the elastic cross-section and the inelastic cross section. The inelastic cross section receives contributions from single and double diffraction. The remainder of the inelastic cross section is referred to as the "hard core" component. Minimum bias events typically contain some single and double diffraction as well as most of the "hard core" component of the inelastic cross section. The "hard core" component does not always correspond to a "hard scattering". Quite often the hadrons ooze through each other and fall apart without any "hard" collisions occurring in the event (*e.g.*, all momentum transfers below a few GeV/c). At the Tevatron about 1% of min-bias events contain a jet with 10 GeV transverse energy. At the LHC we expect the fraction of MB events with a 10 GeV jet to increase by more than a factor of 10. We expect about 1% of MB events at the LHC to contain a 20 GeV jet. Understanding and modeling the jet structure of MB events is crucial at the LHC because of the large amount of pile-up expected.

The UE in a hadron-hadron interaction is everything else accompanying the hard scattering component of the collision.

The CDF UE analysis [1, 2] showed that the density of particles in the UE in jet events is about a factor of two larger than the density of particles in a typical MB collision. At the LHC the difference might be even greater.

Multiple parton interactions (MPI) models [3], extending the QCD perturbative picture to the soft regime, turn out to be particularly adequate to describe the physics of MB and UE. In the framework of these models one can regard the observed differences between the UE in a hard scattering process and a MB collision as the effect of the increased probability of partonic interactions for small impact parameter hadron-hadron collisions (one hard scattering implies a small impact parameter collision which makes it more likely that an additional parton-parton

1

interaction will occur). Also, a hard scattering promotes initial and final state gluon radiation which inevitably contributes to the underlying event.

Hard scattering collider events have a distinct topology and one can use the topological structure of the collision to define regions of η-ϕ space that are sensitive to the UE components of the interaction. By comparing different processes such as high transverse momentum jets, back-to-back dijet production, and the Drell-Yan process both at the Z-boson mass and as a function of the lepton-pair invariant mass, one can partially isolate the various components contributing to the UE.

3   The Tevatron legacy and the status of QCD models

Examples of MPI models are implemented in the general purpose simulation programs PYTHIA [5], JIMMY [6] and SHERPA [7]. Other successful descriptions of UE and MB at hadron colliders are achieved by alternative approaches like PHOJET [8], which rely on both perturbative QCD and Dual Parton Models (DPM). The purely phenomenological UE and MB description available in HERWIG [9] provides a very useful reference of a model not implementing multiple interactions.

Huge progress in the phenomenological study of the underlying event in jet events has been achieved by the CDF experiment at the Tevatron [1, 2], using the multiplicity and transverse momentum spectra of charged tracks in different regions in the azimuth-pseudorapidity space defined with respect to the direction of the leading jet. Regions of the energy flow that receive contributions only by the underlying event have been identified. The average charged multiplicity density in these regions turns out to be significantly higher with respect to the one measured in minimum bias events. This effect, referred to as "pedestal effect", is well reproduced only by varying impact parameters models with correlated parton-parton interactions. Simpler models seem to be ruled out.

As a new tool for the description of UE and MB we would like to mention PYTHIA 6.3 [10], that allows for new interesting features, including the new p_T-ordered initial- and final-state showers and a new very sophisticated multiple interactions model that achieves a description of the colliding partons in the proton in terms of correlated multi-parton distribution functions of flavours, colors and longitudinal momenta.

All these models have to be tested and tuned at the LHC, in particular for what concerns the energy dependent parameters.

4   The Measurement Plan at the LHC

4.1   The Underlying Event as Observed in Charged Jet Events

One can use the topological structure of hadron-hadron collisions to study the UE. Furthermore, this can be done by looking only at the outgoing charged particles [1]. Jets are constructed from the charged particles using a simple clustering algorithm and then the direction of the leading charged particle jet is used to isolate regions of η-ϕ space that are sensitive to the UE. As illustrated in Fig. 1, the direction of the leading charged particle jet, chgjet1, is used to define correlations in the azimuthal angle, $\Delta\phi$. The angle $\Delta\phi = \phi - \phi_{\mathrm{chgjet1}}$ is the relative azimuthal

angle between a charged particle and the direction of chgjet1. The transverse region is almost perpendicular to the plane of the hard 2-to-2 scattering and is therefore very sensitive to the UE. We restrict ourselves to charged particles in the central region $|\eta| < 1$ and consider two p_T thresholds, the nominal CMS cut $p_T > 0.9\,\text{GeV/c}$ and a lower threshold with $p_T > 0.5\,\text{GeV/c}$.

Ultimately we would like to disentangle the hard initial and final state radiation (*i.e.*, multijet production) component of the UE from the beam-beam remnants and MPI components. This can be done by separating the various jet topologies. First one considers events with at least one jet and uses the leading jet direction to define the transverse region (referred to as leading jet events). Of course some of these leading jet events contain multijets that contribute to the activity in the transverse region. Next one considers back-to-back dijet events which are a subset of the leading jet events. The transverse region for the back-to-back dijet events contains much less hard initial and final state radiation and by comparing the two classes of events one can learn about gluon radiation as well as the beam-beam remnants and the MPI component. In this note we will only discuss the leading jet events.
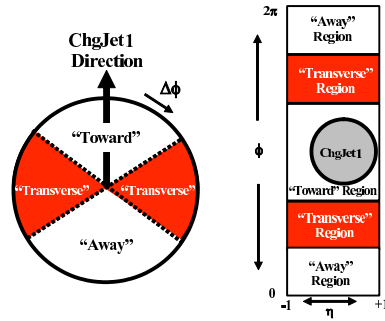

Figure 1: Illustration of correlations in azimuthal angle ϕ relative to the direction of the leading charged particle jet (with cone size $R = 0.7$) in the event, chgjet1. The angle $\Delta\phi = \phi - \phi_{\text{chgjet1}}$ is the relative azimuthal angle between charged particles and the direction of chgjet1. The "transverse" region is defined by $60° < |\Delta\phi| < 120°$ and $|\eta| < 1$. We examine charged particles in the range $|\eta| < 1$ with $p_T > 0.5\,\text{GeV/c}$ or $p_T > 0.9\,\text{GeV/c}$.

Figure 2 and Fig. 3 show the QCD Monte-Carlo models predictions for the average density of charged particles, $dN/d\eta d\phi$, and the average charged PT_{sum} density, $dPT/d\eta d\phi$, respectively, in the transverse region for $|\eta| < 1$ with $p_T > 0.5\,\text{GeV/c}$ and $p_T > 0.9\,\text{GeV/c}$ versus the transverse momentum of the leading charged particle jet. Figure 4 and Fig. 5 are the same as Fig. 2 and Fig. 3, respectively, but with a larger range of the leading charged particle jet transverse momentum. The charged particle density is constructed by dividing the average number of charged particles per event by the area in η-ϕ space (in this case $4\pi/3$). The charged PT_{sum} density is the average scalar p_T sum of charged particles per event divided by the area in η-ϕ space. Working with densities allows one to compare regions of η-ϕ space with different areas. In the future we plan to study the average charged particle p_T and the average maximum charged particle p_T, but we have not included these observables in this note.

The QCD models are HERWIG (without MPI) and two versions of PYTHIA 6.2 (with MPI). One of the PYTHIA versions is the ATLAS tune [11] and the other (Tune DW) is a tune by R. Field which is similar to Tune A [12]. Both Tune A and Tune DW fit the CDF Run 1 and Run 2 UE data [1, 2], but Tune DW also fits the CDF Run 1 Z-boson transverse momentum distribution [4]. Also, both Tune A and Tune DW use the same MPI energy dependence parameter PARP(90) = 0.25, while the ATLAS tune uses the default value of 0.16. Table 1 gives

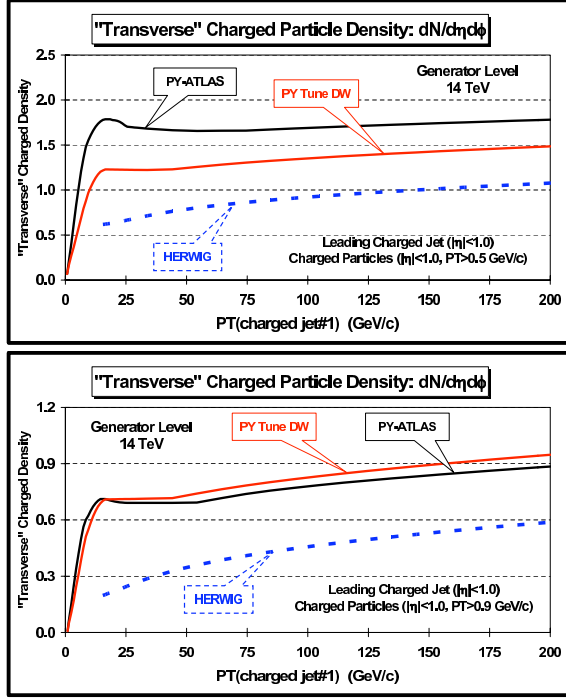Figure 2: QCD Monte-Carlo models predictions for charged particle jet production at $14\,\mathrm{TeV}$. Observables in the transverse region. Average density of charged particles, $dN/d\eta d\phi$, with $|\eta| < 1$ and ptlcut (*top*) or $p_T > 0.9\,\mathrm{GeV/c}$ (*bottom*) versus the transverse momentum of the leading charged particle jet. The QCD models are HERWIG (without MPI) and two versions of PYTHIA 6.2 (with MPI).

the parameters for the various versions of PYTHIA 6.2 which use the CTEQ5L [13] parton distribution function set. Tune DWT is identical to Tune DW at the Tevatron (*i.e.*, $1.96\,\mathrm{TeV}$), but uses the same MPI energy dependence parameter as the ATLAS tune. We will discuss PYTHIA tunes for the LHC in more detail in a forthcoming CMS note.

Table 1: Set of PYTHIA 6.2 parameters defining the different versions of the model adopted in this study. In all the configurations, the CTEQ5L parton distribution functions are considered.

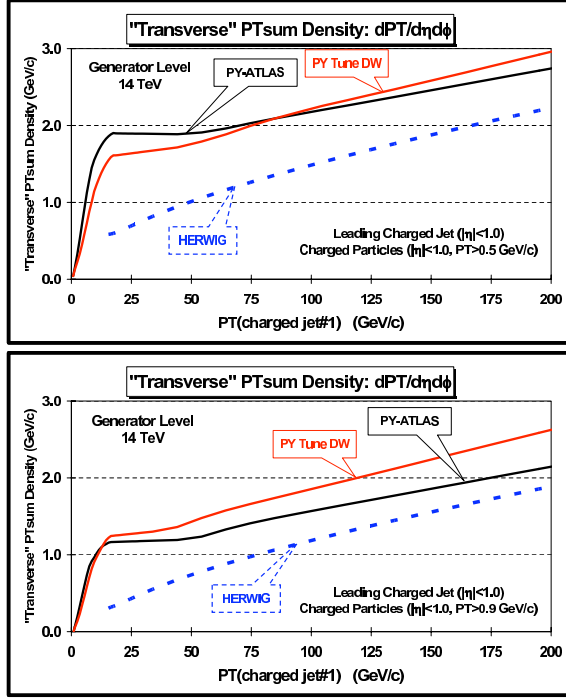| Parameter	Tune A	Tune DW	Tune DWT	ATLAS
MSTP(81)	1	1	1	1
MSTP(82)	4	4	4	4
PARP(82)	$2.0\,\mathrm{GeV}$	$1.9\,\mathrm{GeV}$	$1.9409\,\mathrm{GeV}$	$1.8\,\mathrm{GeV}$
PARP(83)	0.5	0.5	0.5	0.5
PARP(84)	0.4	0.4	0.4	0.5
PARP(85)	0.9	1.0	1.0	0.33
PARP(86)	0.95	1.0	1.0	0.66
PARP(89)	$1.8\,\mathrm{TeV}$	$1.8\,\mathrm{TeV}$	$1.96\,\mathrm{TeV}$	$1.0\,\mathrm{TeV}$
PARP(90)	0.25	0.25	0.16	0.16
PARP(67)	4.0	2.5	2.5	1.0
MSTP(91)	1	1	1	1
PARP(91)	1.0	2.1	2.1	1.0
PARP(93)	5.0	15.0	15.0	5.0

Figure 3: QCD Monte-Carlo models predictions for charged particle jet production at $14\,\mathrm{TeV}$. transverse region: average charged PT_{sum} density, $dPT/d\eta d\phi$, with $|\eta| < 1$ and ptlcut (*top*) or $p_T > 0.9\,\mathrm{GeV/c}$ (*bottom*) versus the transverse momentum of the leading charged particle jet. The QCD models are HERWIG (without MPI) and two versions of PYTHIA 6.2 (with MPI).

The charged jet p_T range 0 to $200\,\mathrm{GeV/c}$ shown in Figs. 2 and 3 is quite interesting. The two versions of PYTHIA (with MPI) behave much differently than HERWIG (without MPI). Due to the MPI the PYTHIA tunes rise rapidly and then reach an approximately flat "plateau" region at $P_T(\mathrm{chgjet1}) \approx 20\,\mathrm{GeV/c}$. Then at $P_T(\mathrm{chgjet1}) \approx 50\,\mathrm{GeV/c}$ they begin to rise again due to initial and final state radiation which increases as the Q^2 scale of the hard scattering increases. The rise is more evident for the high p_T threshold $p_T > 0.9\,\mathrm{GeV/c}$. HERWIG has considerably fewer particles in the transverse region and predicts a steady rise over this region resulting from initial and final state radiation. The ATLAS tune predicts a larger charged particle density in the transverse region than Tune DW for $p_T > 0.5\,\mathrm{GeV/c}$. However, the ATLAS tune and Tune DW are have similar charged particle densities in the transverse region for $p_T > 0.9\,\mathrm{GeV/c}$. This is because the ATLAS tune has a "softer" charged particle p_T distribution than Tune DW.

Figure 6 shows the p_T dependence of the average density of charged particles, $dN/d\eta d\phi dp_T$, with $|\eta| < 1$ in the transverse region for leading charged particle jets with $P_T(\mathrm{chgjet1}) > 120\,\mathrm{GeV/c}$. The integral of $dN/d\eta d\phi dp_T$ over the range $p_T > 0.5\,\mathrm{GeV/c}$ or $p_T > 0.9\,\mathrm{GeV/c}$ corresponds to the average density of charged particles, $dN/d\eta d\phi$, shown in Fig. 2. One can clearly see that both HERWIG and the ATLAS tune have a "softer" distribution of charged particles than Tune DW.

Figure 7 shows the average density of charged particles, $dN/d\eta d\phi$, with $p_T > p_T^{min}$ and $|\eta| < 1$ in the transverse region for leading charged particle jets with $P_T(\mathrm{chgjet1}) > 120\,\mathrm{GeV/c}$. Figure 7 also shows the ratio of charged particles with $p_T > p_T^{min}$ to the total number of charged particles in the transverse region with $|\eta| < 1$. According to Tune DW, about 38% of the charged particles are retained by the nominal selection cut $p_T > 0.9\,\mathrm{GeV/c}$, while the selection efficiency
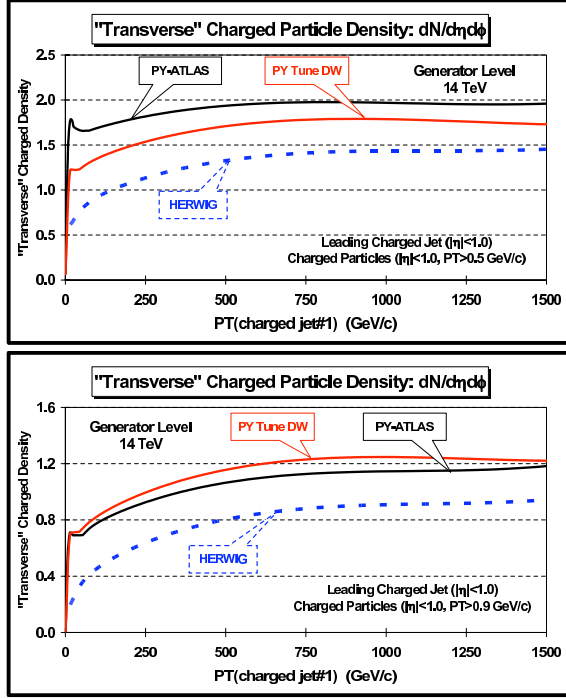
Figure 4: The same as Fig. 2 but with a larger range of the leading charged particle jet transverse momentum. QCD Monte-Carlo models predictions for charged particle jet production at $14\,\mathrm{TeV}$. Observables in the transverse region. Average density of charged particles, $dN/d\eta d\phi$, with $|\eta| < 1$ and ptlcut (*top*) or $p_T > 0.9\,\mathrm{GeV/c}$ (*bottom*) versus the transverse momentum of the leading charged particle jet. The QCD models are HERWIG (without MPI) and two versions of PYTHIA 6.2 (with MPI).

for HERWIG and for the ATLAS tune drop to 24% and 22%, respectively. Lowering the cut on charged particles to $p_T > 0.5\,\mathrm{GeV/c}$, the selection efficiency figures rise to 60% for Tune DW and to 45% for both HERWIG and the ATLAS tune.

Figure 8 shows the statistical errors on the average charged particle density in the transverse region for an integrated luminosity of $100\,\mathrm{nb}^{-1}$ and an integrated luminosity of $100\,\mathrm{pb}^{-1}$. Of course, higher integrated luminosity results in more events per bin and hence a smaller statistical error. The range $0 < P_T(\mathrm{chgjet1}) < 200\,\mathrm{GeV/c}$ can be measured accurately with $100\,\mathrm{nb}^{-1}$, while with $100\,\mathrm{pb}^{-1}$ one can study charged particle jets up to about $1\,\mathrm{TeV/c}$.

These figures obviously do not take into account the inefficiencies and the unavoidable prescaling which have to be applied to triggers selecting high rate processes. Assuming to allocate a $1\,Hz$ final rate to a minimum bias stream in nominal CMS conditions, would imply a pre-scaling factor of 4×10^7. For this reason, in order to study the range $0 < P_T(\mathrm{chgjet1}) < 200\,\mathrm{GeV/c}$, it will be necessary to use both minimum bias and high p_T triggers, the latter being characterized by much lower pre-scaling factors.

4.2 The Underlying Event as Observed in Drell-Yan Muon-Pair Production

Drell-Yan muon pair production provides an excellent way to study the UE. Here one studies the outgoing charged particles (excluding the $\mu^+\mu^-$ pair) as a function of the muon-pair invariant mass. After removing the muon-pair everything else is the UE (*i.e.*, initial-state radiation, beam-
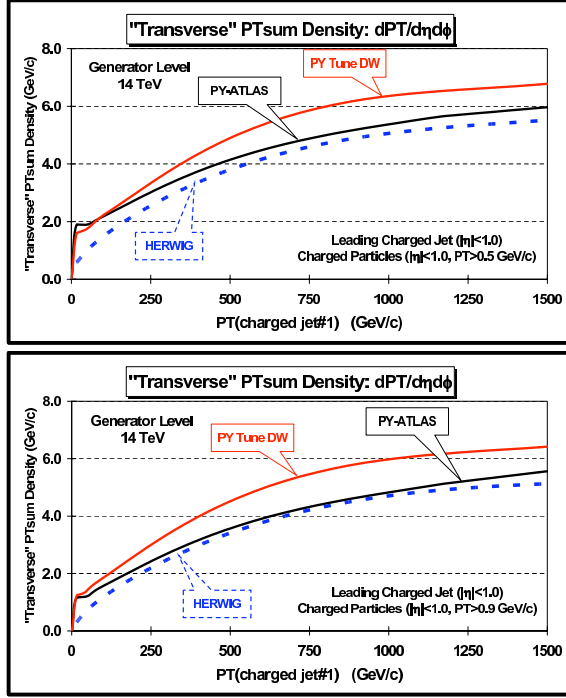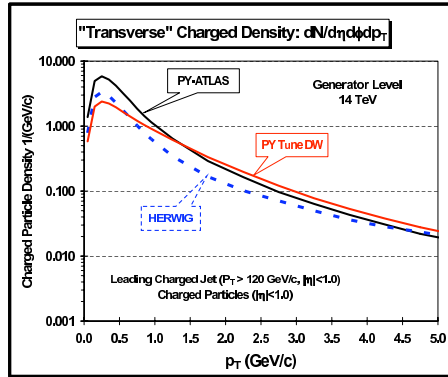
Figure 5: The same as Fig. 3 but with a larger range of the leading charged particle jet transverse momentum. QCD Monte-Carlo models predictions for charged particle jet production at $14\,\mathrm{TeV}$. Observables in the transverse region. Average charged PT_{sum} density, $dPT/d\eta d\phi$, with $|\eta| < 1$ and ptlcut (*top*) or $p_T > 0.9\,\mathrm{GeV/c}$ (*bottom*) versus the transverse momentum of the leading charged particle jet. The QCD models are HERWIG (without MPI) and two versions of PYTHIA 6.2 (with MPI).

Figure 6: QCD Monte-Carlo models predictions for charged particle jet production at $14\,\mathrm{TeV}$. Observables in the transverse region. p_T dependence of density of charged particles, $dN/d\eta d\phi dp_T$, with $|\eta| < 1$ for leading charged particle jets with $P_T(\mathrm{chgjet1}) > 120\,\mathrm{GeV/c}$. The QCD models are HERWIG (without MPI) and two versions of PYTHIA 6.2 (with MPI).

beam remnants, and MPI). As for the charged jet production, we restrict ourselves to charged particles in the central region $|\eta| < 1$ and consider the two p_T thresholds $p_T > 0.5\,\mathrm{GeV/c}$ and $p_T > 0.9\,\mathrm{GeV/c}$.

Figures 9 and 10 show the QCD Monte-Carlo model predictions for the average charged particle density, $dN/d\eta d\phi$, and the average charged PT_{sum} density, $dPT/d\eta d\phi$ in muon-pair production versus the muon-pair invariant mass. Here the densities are constructed by dividing by 4π.
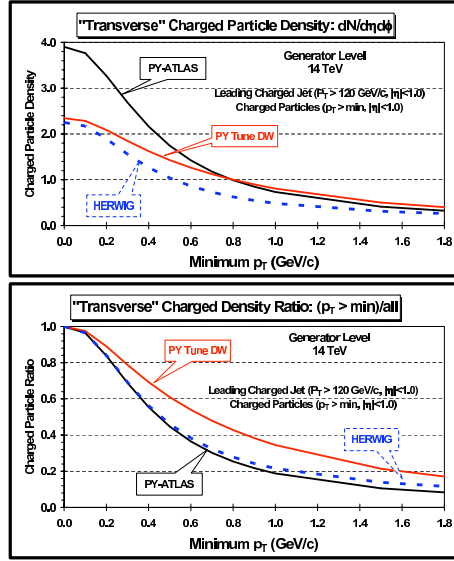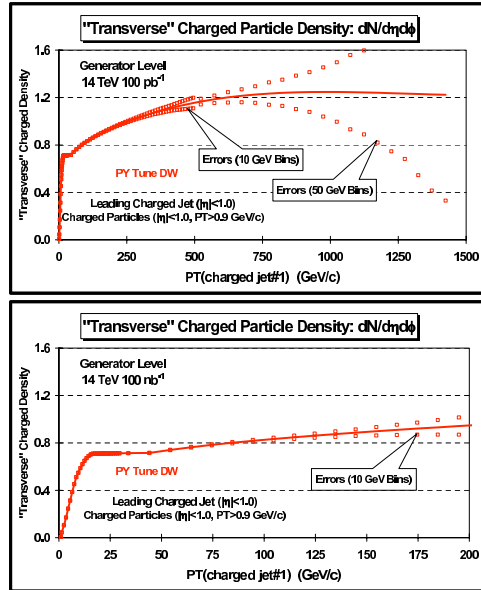
7

Figure 7: QCD Monte-Carlo models predictions for charged particle jet production at $14\,\mathrm{TeV}$. Observables in the transverse region. Average density of charged particles, $dN/d\eta d\phi$, with $p_T > p_T^{min}$ and $|\eta| < 1$ for leading charged particle jets with $P_T(\mathrm{chgjet1}) > 120\,\mathrm{GeV/c}$. (*top*) Average density of charged particles, $dN/d\eta d\phi dp_T$, integrated over the range $p_T > p_T^{min}$. (*bottom*) Ratio of charged particles with $p_T > p_T^{min}$ to the total number of charged particles with $|\eta| < 1$. The QCD models are HERWIG (without MPI) and two versions of PYTHIA 6.2 (with MPI).

Figure 8: QCD Monte-Carlo models predictions for charged particle jet production at $14\,\mathrm{TeV}$. Observables in the transverse region. (*top*) Average density of charged particles, $dN/d\eta d\phi$, with $p_T > 0.9\,\mathrm{GeV/c}$ and $|\eta| < 1$ versus the transverse momentum of the leading charged particle jet for Tune DW together with the statistical errors (10 and $50\,\mathrm{GeV/c}$ bins) for an integrated luminosity of $100\,\mathrm{pb}^{-1}$. (*bottom*) Average density of charged particles, $dN/d\eta d\phi$, with $p_T > 0.9\,\mathrm{GeV/c}$ and $|\eta| < 1$ versus the transverse momentum of the leading charged particle jet for Tune DW together with the statistical errors ($10\,\mathrm{GeV/c}$ bins) for an integrated luminosity of $100\,\mathrm{nb}^{-1}$.

HERWIG (without MPI) produces significantly fewer particles than the PYTHIA tunes (with MPI). By comparing the two thresholds $p_T > 0.5\,\mathrm{GeV/c}$ and $p_T > 0.9\,\mathrm{GeV/c}$, we again see that

the ATLAS tune has a "softer" p_T distribution of charged particles than Tune DW. Figures 9 and 10 also show a third PYTHIA tune (see Table 1). Tune DWT is identical to Tune DW at the Tevatron (*i.e.*, $1.96\,\mathrm{TeV}$) and both describe the CDF UE data. Tune DWT uses the same multiple parton interaction energy dependence parameter, PARP(90) $= 0.16$, as the ATLAS tune (Tune DW uses PARP(90) $= 0.25$). We explain this in more detail in our forthcoming CMS note on PYTHIA tunes for the LHC. PYTHIA Tune DWT predicts a more active UE at the LHC (with $p_T > 0.9\,\mathrm{GeV/c}$) than either Tune DW or the ATLAS tune.
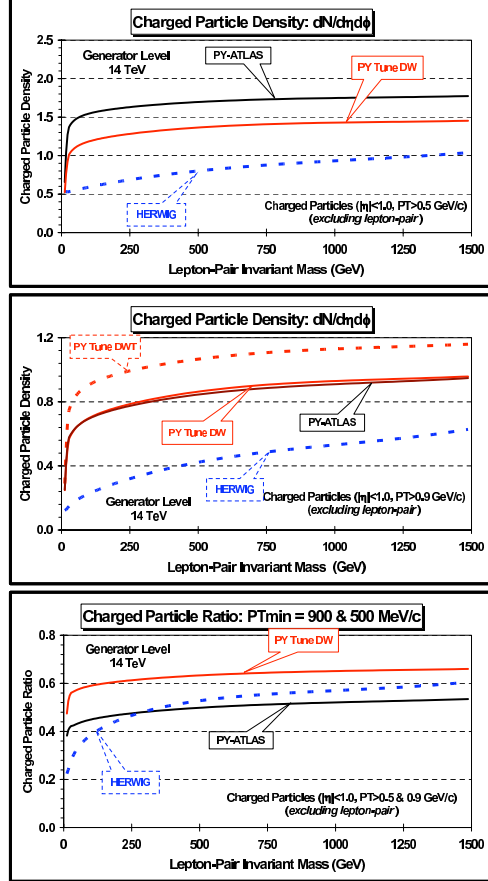
Figure 9: QCD Monte-Carlo models predictions for Drell-Yan muon-pair production at $14\,\mathrm{TeV}$. (*top*) Average charged particle density, $dN/d\eta d\phi$, with $p_T > 0.5\,\mathrm{GeV/c}$ and $|\eta| < 1$ versus the muon-pair invariant mass for Tune DW, ATLAS, and HERWIG (with no MPI). (*middle*) Average charged particle density with $p_T > 0.9\,\mathrm{GeV/c}$ and $|\eta| < 1$ versus the muon-pair invariant mass. (*bottom*) Charged particle ratio $p_T > 0.9\,\mathrm{GeV/c}$ divided by $p_T > 0.5\,\mathrm{GeV/c}$ versus the lepton-pair invariant mass.

Figure 11 shows the p_T dependence of the average density of charged particles, $dN/d\eta d\phi dp_T$, with $|\eta| < 1$ and $70 < M(\mu^+\mu^-) < 110\,\mathrm{GeV}$. The integral of $dN/d\eta d\phi dp_T$ over the range $p_T > 0.5\,\mathrm{GeV/c}$ or $p_T > 0.9\,\mathrm{GeV/c}$ corresponds to the density of charged particles, $dN/d\eta d\phi$, shown in Fig. 9. One can again clearly see that both HERWIG and the ATLAS tune have a "softer" distribution of charged particles than does PYTHIA Tune DW. Figure 12 shows the average density of charged particles, $dN/d\eta d\phi$, with $p_T > p_T^{min}$ with $|\eta| < 1$ and $70 < M(\mu^+\mu^-) < 110\,\mathrm{GeV}$. Figure 12 also shows the ratio of charged particles with $p_T > p_T^{min}$ to the total number of charged particles with $|\eta| < 1$. According to Tune DW, about 35% of the charged particles are retained by the nominal selection cut $p_T > 0.9\,\mathrm{GeV/c}$, while the selection efficiency for HERWIG and for the ATLAS tune drop to 13% and 19%, respectively. Lowering the cut on
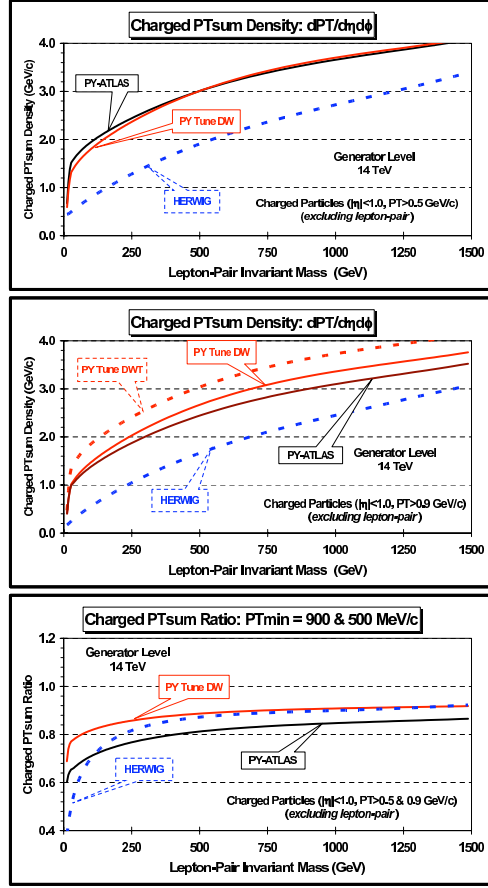
9

Figure 10: QCD Monte-Carlo models predictions for Drell-Yan muon-pair production at $14\,\mathrm{TeV}$. (*top*) Average charged PT_{sum} density, $dPT/d\eta d\phi$, with $p_T > 0.5\,\mathrm{GeV/c}$ and $|\eta| < 1$ versus the muon-pair invariant mass for Tune DW, ATLAS, and HERWIG (with no MPI). (*middle*) Average charged PT_{sum} density with $p_T > 0.9\,\mathrm{GeV/c}$ and $|\eta| < 1$ versus the muon-pair invariant mass. (*bottom*) Charged PT_{sum} ratio $p_T > 0.9\,\mathrm{GeV/c}$ divided by $p_T > 0.5\,\mathrm{GeV/c}$ versus the lepton-pair invariant mass.

charged particles to $p_T > 0.5\,\mathrm{GeV/c}$, the selection efficiency figures rise to 59% for Tune DW and to 35% and 43% for HERWIG and the ATLAS tune, respectively.

Figure 13 shows the statistical errors on the average charged particle density for an integrated luminosity of $100\,\mathrm{pb^{-1}}$. With $100\,\mathrm{pb^{-1}}$ of data we could easily distinguish between HERWIG and PYTHIA Tune DW for muon-pair mass up to roughly $300\,\mathrm{GeV}$.

5   Feasibility studies

Early MB and UE measurements in the pilot run will be reported in vol.3 of the CMS PTDR. Here we concentrate on the UE measurement that will be performed in nominal CMS conditions at low luminosity. All the studies presented in this section and in Appendix A are obtained applying the official full simulation and reconstruction chain of the CMS experiment.

Events corresponding to Drell-Yan di-muon pairs (for different di-muon invariant mass ranges) and to leading order QCD processes (for different p_T ranges of the outcoming partons) are generated with PYTHIA 6.2. The same generator is used in order to simulate the superimposed low luminosity pile-up. The relevant PYTHIA 6.2 parameters adopted by CMS in official pro-
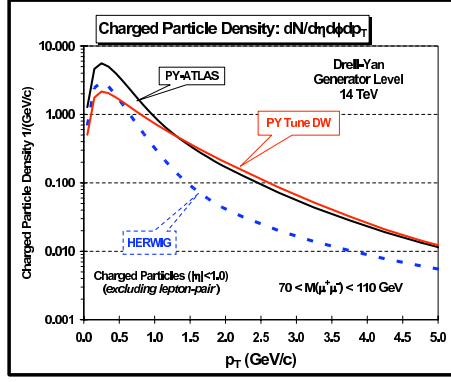
Figure 11: QCD Monte-Carlo models predictions for Drell-Yan muon-pair production at $14\,\text{TeV}$. p_T dependence of density of charged particles, $dN/d\eta d\phi dp_T$, with $|\eta| < 1$ and $70 < M(\mu^+ \mu^-) < 110\,\text{GeV}$. The QCD models are HERWIG (without MPI) and two versions of PYTHIA 6.2 (with MPI).
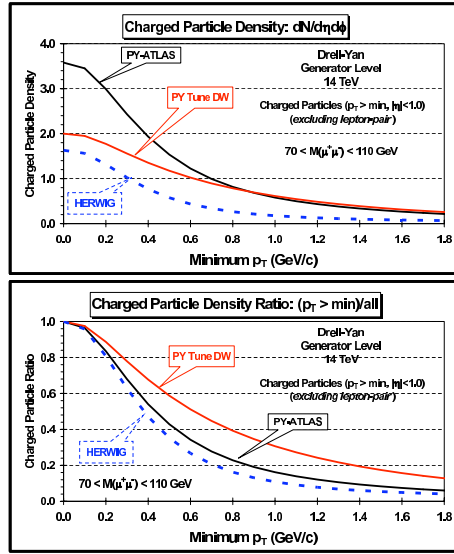

Figure 12: QCD Monte-Carlo models predictions for Drell-Yan muon-pair production at $14\,\text{TeV}$. Average density of charged particles, $dN/d\eta d\phi$, with $p_T > p_T^{min}$ with $|\eta| < 1$ and $70 < M(\mu^+ \mu^-) < 110\,\text{GeV}$. (*top*) Average density of charged particles, $dN/d\eta d\phi dp_T$, integrated over the range $p_T > p_T^{min}$. (*bottom*) Ratio of charged particles with $p_T > p_T^{min}$ to the total number of charged particles with $|\eta| < 1$. The QCD models are HERWIG (without MPI) and two versions of PYTHIA 6.2 (with MPI).

duction are documented in [14]. The triggers used to collect Drell-Yan and Jet samples are described in reference [15]. The definition of the main UE observables are introduced in section 4.

Charged tracks with p_T above $0.9\,\text{GeV/c}$ are reconstructed adopting the procedure described in [16]. The same algorithm is also used with different parameters, which achieve reasonable performances for p_T above $0.5\,\text{GeV/c}$. Details concerning the charged track reconstruction, including the estimation of the expected reconstruction efficiencies and fake rates for both scenarios, are reported in Appendix A. No corrections are applied when comparing reconstruction level to generator level distributions and profiles. Only charged tracks in the central pseudo-rapidity region ($|\eta| < 1$) are considered.
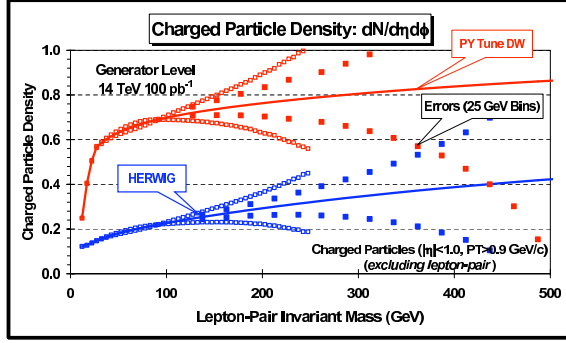
Figure 13: QCD Monte-Carlo models predictions for Drell-Yan muon-pair production at $14\,\mathrm{TeV}$. Average charged particle density, $dN/d\eta d\phi$, with $p_T > 0.9\,\mathrm{GeV/c}$ and $|\eta| < 1$ versus the muon-pair invariant mass for Tune DW, and HERWIG together with the statistical errors (10 and $25\,\mathrm{GeV/c}$ bins) for an integrated luminosity of 100 pb^{-1}.

5.1 Measurement of the Underlying Event in jet events

The scale of the leading interaction can be quoted in many different ways. The tracker-based measurement allows to keep an acceptable resolution for jet energies below $20\,\mathrm{GeV}$, where the calorimetric measurement is dominated by large systematic uncertainties. The p_T calibration and the resolution of the leading charged jet are reported in Fig. 14.
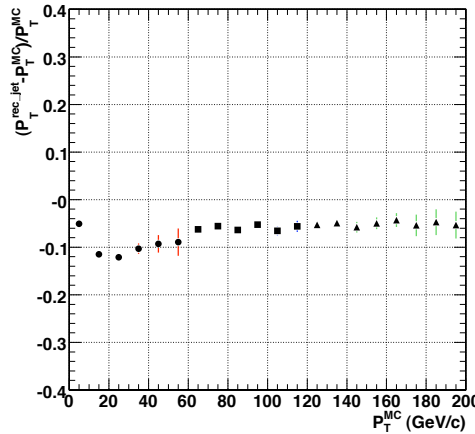
Figure 14: Relative p_T shift of the reconstructed leading charged jet with respect to the same object defined at generator level. Error bars indicate the resolution.

In principle MB could be studied from any stream, getting rid of the leading pp interaction and embarking the reconstruction of all the primary vertices from all the other piled-up pp interactions. However this methodology turns out to be challenging as the resolution on the position of the pp vertices degrades when lowering the total p_T of the associated charged tracks. A methodology to optimize MB study from piled-up interactions will be presented in a dedicated CMS note. In this study, a MB trigger is defined requiring at least a calorimetric jet of $p_T > 20\,\mathrm{GeV/c}$. In order to combine the measurements performed at different leading charged jet scales, on top of the MB trigger, two additional triggers based on the p_T of the leading high level trigger jet are adopted: $p_T > 60$ GeV/c and $p_T > 120\,\mathrm{GeV/c}$, which will be referred to as JET60 and JET120. These calorimetric jets are reconstructed with an iterative cone algorithm of radius 0.5 in the pseudorapidity-azimuth space.

12

The distance between the leading charged jet and the leading calorimetric jet in the pseudorapidity-azimuth space is reported in Fig. 15. Two different contributions are clearly seen: a narrow peak around zero that is due to the events where the charged jet turns out to be well matched to the leading calorimetric jet, and a wider distribution which accounts for the events where the directions of the charged and calorimetric jets are uncorrelated.
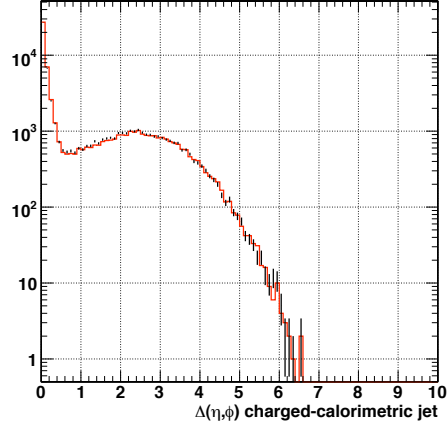

Figure 15: Distance in the space $\eta - \phi$ between the reconstructed leading calorimetric jet and the reconstructed leading charged jet (*points*); distance between the reconstructed leading calorimetric jet and the generator level leading charged jet (*histogram*).
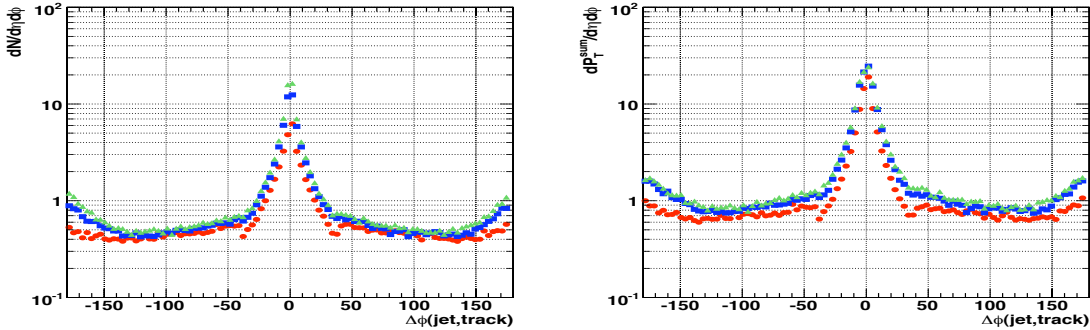
Figure 16: Charged jet production at $14\,\mathrm{TeV}$. Density of charged particles, $dN/d\eta d\phi$ (*left*) and average charged PT_{sum} density, $dPT/d\eta d\phi$ (*right*), with $p_T > 0.9\,\mathrm{GeV/c}$ and $|\eta| < 1$ versus the azimuthal distance between charged tracks and leading charged jet. Data from different triggers are superimposed: (*red circles*) = Minimum Bias; (*blue squares*) = JET60; (*green triangles*) = JET120. All the distributions are at reconstruction level and uncorrected.

Tracks arising from the piled-up interactions are suppressed requiring the extrapolated coordinate along the beam axis to be inside $1mm$ with respect to the primary vertex associated to the leading charged jet. The selection of the pp interaction with the highest p_T charged jet tends to create a small bias on the MB sample, reducing the statistics available for low p_T charged jets. In principle this problem could be solved studying in detail each pp interaction, however such refinement is not implemented in the analysis presented here, due to the additional complications and systematics connected to the parameterizations of the corrections.

Figure 16 reports $dN/d\eta d\phi$, and the average charged PT_{sum} density, $dPT/d\eta d\phi$, with $p_T > 0.9\,\mathrm{GeV/c}$ and $|\eta| < 1$ versus the azimuthal distance between charged tracks and the leading charged jet for the data from the three different triggers introduced above. The enhanced activity

13

due to the presence of the leading charged jet in the toward region (at 0 degrees) can be clearly identified, along with the rise in the away region (± 180 degrees) which is due to the recoiling jet. The transverse region (centered at ± 90 degrees) is characterized by the lowest activity and flat distributions, as expected. Little dips at ± 40 degrees are seen, which are particularly clear for the MB stream. This effect, that is less sensitive at higher p_T, has been already observed in the CDF data. It is due to the jet clustering algorithm, and It appears as if the particles are "sucked" into the jet.

The density of charged particles, $dN/d\eta d\phi$, and the average charged PT_{sum} density, $dPT/d\eta d\phi$, with $p_T > 0.9\,\text{GeV/c}$ and $|\eta| < 1$ in toward and transverse regions are reported in Figs. 17 and 18, respectively. $2\,\text{GeV/c}$ bins are used up to $P_T(\text{chgjet1}) = 20\,\text{GeV/c}$, $10\,\text{GeV/c}$ bins above such threshold. The same observables in the transverse region with $p_T > 0.5\,\text{GeV/c}$ and $|\eta| < 1$ are reported in Fig. 19.

The shapes of uncorrected reconstruction level distributions basically agree with the corresponding generator level ones. The difference in absolute scale (about -20% for both $dN/d\eta d\phi$ and $dPT/d\eta d\phi$) turns out to be compatible with charged jet energy calibration, charged track inefficiencies and charged track fake rates (see Appendix A).
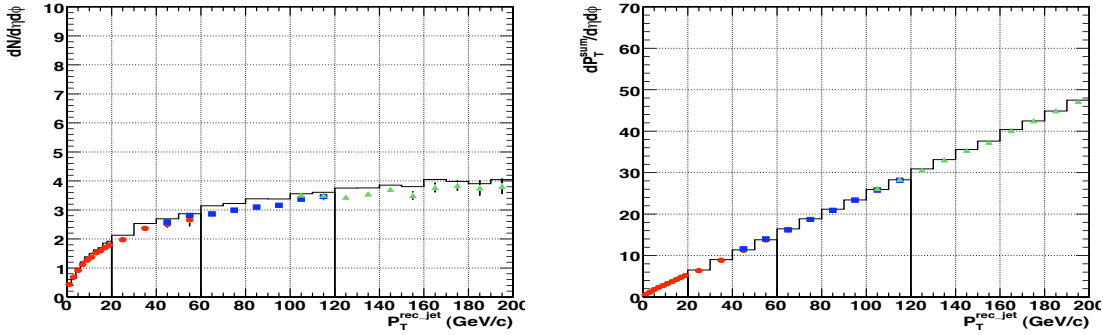

Figure 17: Charged jet production at $14\,\text{TeV}$. Density of charged particles, $dN/d\eta d\phi$ (*left*) and average charged PT_{sum} density, $dPT/d\eta d\phi$ (*right*), with $p_T > 0.9\,\text{GeV/c}$ and $|\eta| < 1$ in the toward region versus the transverse momentum of the leading charged particle jet. Data from different triggers are superimposed: (*red squares*) = Minimum Bias; (*blue circles*) = JET60; (*green triangles*) = JET120. (*points*) correspond to the raw (uncorrected) reconstruction level profiles; (*histograms*) correspond to the generator level profiles for the events passing the reconstruction level selection.

Figure 20 reports the ratio between the observables for $p_T > 0.9\,\text{GeV/c}$ and $p_T > 0.5\,\text{GeV/c}$ in transverse region. Lowering the p_T threshold in track reconstruction to $0.5\,\text{GeV/c}$ allows to recover about 50% of the multiplicity and about 30% of the transverse momentum associated to the charged tracks. These ratios, which are sensitive to differences between different models and/or different tunings, are also nicely free from the systematic effects enumerated above, and basically don't need to be corrected when comparing to the corresponding generator level obervables.

5.2 The Underlying Event in muon-pair events

The scale of the Drell-Yan process can be quantified using the invariant mass or the p_T of the two muons, whose measurement relies on both muon and tracker stations. While muon reconstruction is made in the full CMS acceptance (pseudorapidity between -2.4 and 2.4), in order to keep an adequate efficiency and fake rate, charged track reconstruction for the measurement
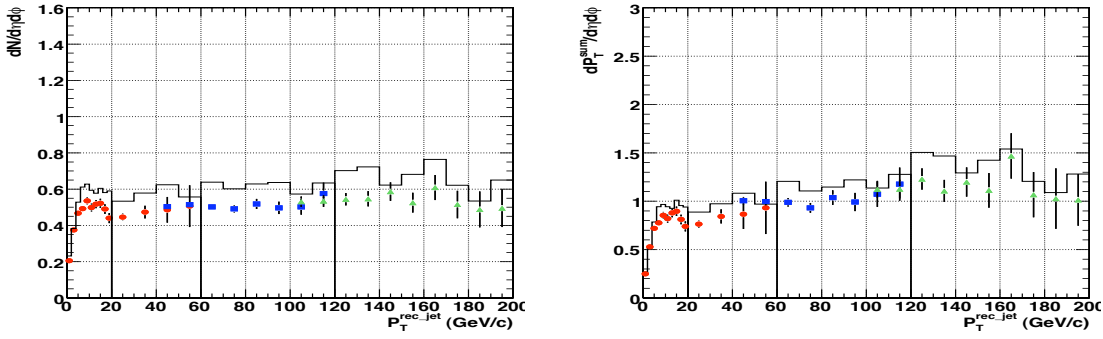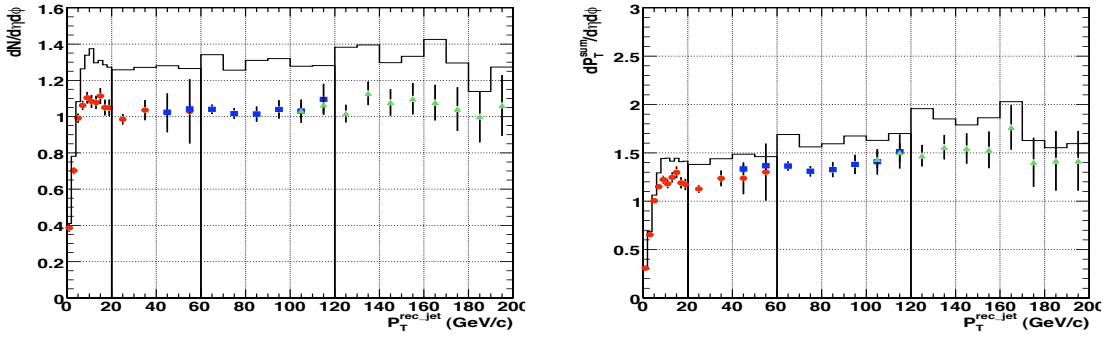
14

Figure 18: Charged jet production at $14\,\text{TeV}$. Density of charged particles, $dN/d\eta d\phi$ (*left*) and average charged PT_{sum} density, $dPT/d\eta d\phi$ (*right*), with $p_T > 0.9\,\text{GeV/c}$ and $|\eta| < 1$ in the transverse region versus the transverse momentum of the leading charged particle jet. Data from different triggers are superimposed: (*red squares*) = Minimum Bias; (*blue circles*) = JET60; (*green triangles*) = JET120.(*points*) correspond to the raw (uncorrected) reconstruction level profiles; (*histograms*) correspond to the generator level profiles for the events passing the reconstruction level selection.

Figure 19: Charged jet production at $14\,\text{TeV}$. Density of charged particles, $dN/d\eta d\phi$ (*left*) and average charged PT_{sum} density, $dPT/d\eta d\phi$ (*right*), with $p_T > 0.5\,\text{GeV/c}$ and $|\eta| < 1$ in the transverse region versus the transverse momentum of the leading charged particle jet. Data from different triggers are superimposed: (*red squares*) = Minimum Bias; (*blue circles*) = JET60; (*green triangles*) = JET120. (*points*) correspond to the raw (uncorrected) reconstruction level profiles; (*histograms*) correspond to the generator level profiles for the events passing the reconstruction level selection.

of the event activity is made in the central region (pseudorapidity between -1.0 and 1.0), along the lines of the UE study for jets reported in the previous section. Drell-Yan event topology is such that all the activity observed in the overall azimuth range (excluding the two leading muons) can be interpreted as the contribution of the Underlying Event, hence, in contrast to the UE study for jets, there's no need to quote the observables in different sub-regions.

The relative mass shift and the corresponding resolution of the reconstructed muon-pair are reported in Fig. 21. The resolution outside the Z peak is dominated by the lack of Monte Carlo statistics. Single muon and muon-pair CMS triggers insure very high efficiencies for the studied process [17].

Tracks arising from the piled-up interactions are suppressed requiring the extrapolated coordinate along the beam axis to be inside $1mm$ with respect to the primary vertex associated to the leading muons.

The charged particle density, $dN/d\eta d\phi$, and the average charged PT_{sum} density, $dPT/d\eta d\phi$ with $p_T > 0.9\,\text{GeV/c}$ and $|\eta| < 1$ in muon-pair production versus the muon-pair invariant mass
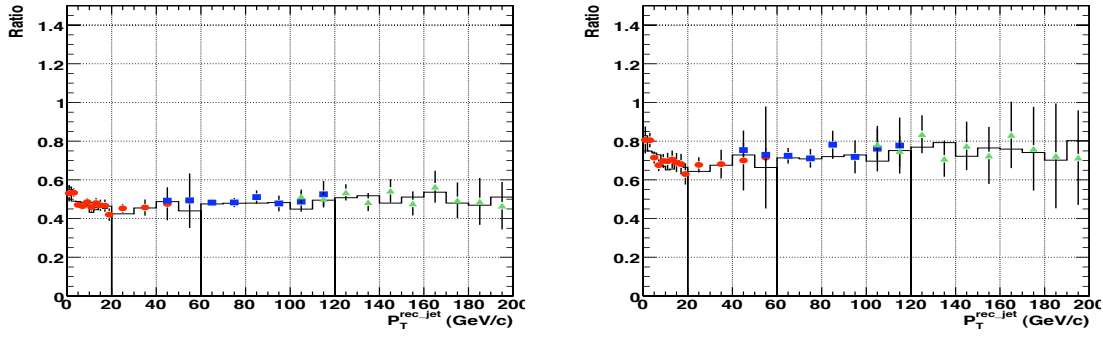
Figure 20: Charged jet production at $14\,\mathrm{TeV}$. Charged tracks in the transverse region. (*left*) = Ratio between density of charged particles with $p_T > 0.9\,\mathrm{GeV/c}$ and $p_T > 0.5\,\mathrm{GeV/c}$ versus the transverse momentum of the leading charged particle jet. (*right*) = Ratio between average charged PT_{sum} density with $p_T > 0.9\,\mathrm{GeV/c}$ and $p_T > 0.5\,\mathrm{GeV/c}$ versus the transverse momentum of the leading charged particle jet. Data from different triggers are superimposed: (*red squares*) = Minimum Bias; (*blue circles*) = JET60; (*green triangles*) = JET120. (*points*) correspond to the raw (uncorrected) reconstruction level profiles; (*histograms*) correspond to the generator level profiles for the events passing the reconstruction level selection.
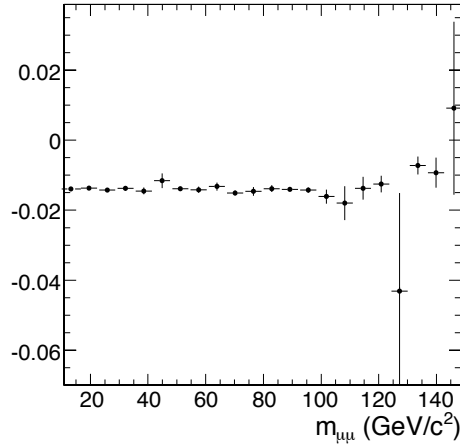
Figure 21: Muon-pair production at $14\,\mathrm{TeV}$. Relative mass shift of the reconstructed muon-pair invariant mass with respect to the same object defined at generator level. Error bars indicate the resolution.
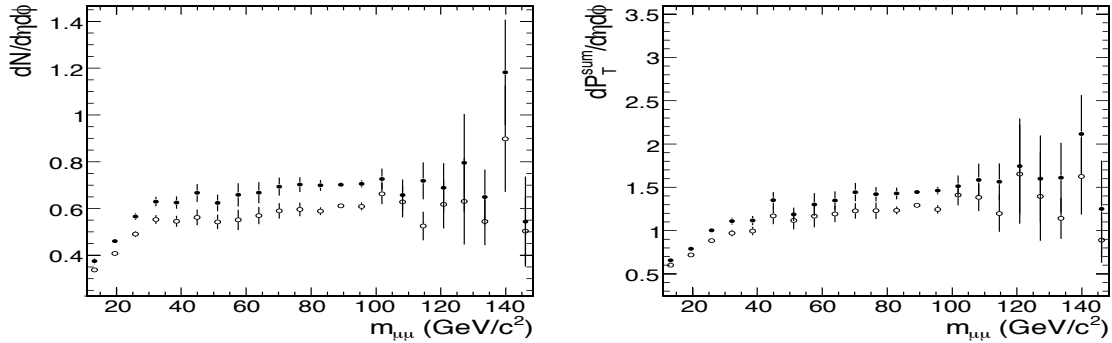
are reported in Fig. 22.

Figure 22: Muon-pair production at $14\,\mathrm{TeV}$. Density of charged particles, $dN/d\eta d\phi$ (*left*) and average charged PT_{sum} density, $dPT/d\eta d\phi$ (*right*), with $p_T > 0.9\,\mathrm{GeV/c}$ and $|\eta| < 1$ versus the muon-pair invariant mass. (*empty circles*) correspond to the raw (uncorrected) reconstruction level profiles; (*full circles*) correspond to the generator level profiles for the events passing the reconstruction level selection.
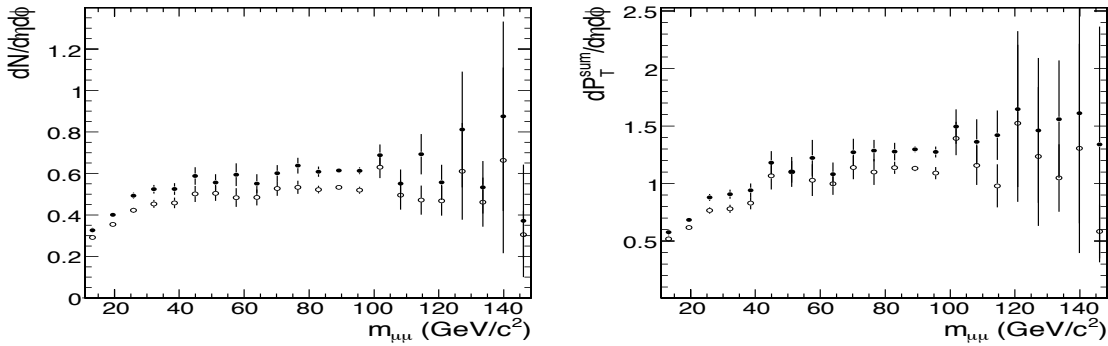
16

Figure 23: Muon-pair production at $14\,\mathrm{TeV}$ with two isolated muons. Density of charged particles, $dN/d\eta d\phi$ (*left*) and average charged PT_{sum} density, $dPT/d\eta d\phi$ (*right*), with $p_T > 0.9\,\mathrm{GeV/c}$ and $|\eta| < 1$ versus the muon-pair invariant mass. (*empty circles*) correspond to the raw (uncorrected) reconstruction level profiles; (*full circles*) correspond to the generator level profiles for the events passing the reconstruction level selection.

In our study, we require "isolated muons" not to have charged tracks with $p_T > 0.9\,\mathrm{GeV/c}$ in a cone of radius 0.3 in the azimuth-pseudorapidity space centered along the direction of the muon. Selecting isolated muons turns out to be essential in order to reduce the QCD background to negligible levels for $p_T > 15\,\mathrm{GeV/c}$, while keeping an efficiency of 76.9% for Drell-Yan muon-pairs in the same p_T region.

The charged particle density, $dN/d\eta d\phi$, and the average charged PT_{sum} density, $dPT/d\eta d\phi$ with $p_T > 0.9\,\mathrm{GeV/c}$ and $|\eta| < 1$ in muon-pair production with isolated muons versus the muon-pair invariant mass are reported in Fig. 23. The sensitive decrease of both these observables depend on the correlations between the isolation and the underlying event activity [18].

6   Conclusions

Predictions on the amount of activity in UE at the LHC based on extrapolations from the lower energy data differ greatly. In this study we have demonstrated the feasibility of reference UE measurements at CMS under nominal conditions, assessing our capability to distinguish between the predictions of different models. The UE is studied by examining charged particles in the transverse region in charged particle jet production and in the central region of Drell-Yan muon-pair production (after removing the muon-pair).

7   Acknowledgments

References

[1] A. A. Affolder *et al.* [CDF Collaboration], "Charged jet evolution and the underlying event in proton anti-proton collisions at 1.8-TeV," Phys. Rev. D **65** (2002) 092002.

[2] D. Acosta *et al.* [CDF Collaboration], "The underlying event in hard interactions at the Tevatron anti-p p collider," Phys. Rev. D **70** (2004) 072002 [arXiv:hep-ex/0404004].

17

[3] T. Sjostrand and M. van Zijl, "Multiple Parton-Parton Interactions in an Impact Parameter Picture," Phys. Lett. B **188** (1987) 149.

[4] F. Abe *et al.* [CDF Collaboration], "Measurement of the Z (p(T)) distribution in anti-p p collisions at s**(1/2) = 1.8-TeV," Phys. Rev. Lett. **67** (1991) 2937.

[5] T. Sjostrand, P. Eden, C. Friberg, L. Lonnblad, G. Miu, S. Mrenna and E. Norrbin, "High-energy-physics event generation with PYTHIA 6.1," Comput. Phys. Commun. **135** (2001) 238 [arXiv:hep-ph/0010017].

[6] J. M. Butterworth, J. R. Forshaw and M. H. Seymour, "Multiparton interactions in photo-production at HERA," Z. Phys. C **72** (1996) 637 [arXiv:hep-ph/9601371].

[7] T. Gleisberg, S. Hoche, F. Krauss, A. Schalicke, S. Schumann and J. C. Winter, "SHERPA 1.alpha, a proof-of-concept version," JHEP **0402** (2004) 056 [arXiv:hep-ph/0311263].

[8] F. W. Bopp, R. Engel and J. Ranft, "Rapidity gaps and the PHOJET Monte Carlo," arXiv:hep-ph/9803437.

[9] G. Corcella *et al.*, "HERWIG 6: An event generator for hadron emission reactions with interfering gluons (including supersymmetric processes)," JHEP **0101** (2001) 010 [arXiv:hep-ph/0011363].

[10] T. Sjostrand and P. Z. Skands, "Transverse-momentum-ordered showers and interleaved multiple interactions," Eur. Phys. J. C **39** (2005) 129 [arXiv:hep-ph/0408302].

[11] C. M. Buttar, D. Clements, I. Dawson and A. Moraes, "Simulations of minimum bias events and the underlying event, MC tuning and predictions for the LHC," Acta Phys. Polon. B **35** (2004) 433.

[12] R. Field [CDF Collaboration], "Min-bias and the underlying event in Run 2 at CDF," Acta Phys. Polon. B **36** (2005) 167.

[13] The CTEQ Collaboration, "Global QCD Analysis of Parton Structure of the Nucleon: CTEQ5 Parton Distributions," Eur. Phys. J. **C12**, 375-392, 2000.

[14] P. Bartalini, R. Chierici and A. De Roeck, "Guidelines for the estimation of theoretical uncertainties at the LHC," CERN-CMS-NOTE-2005-013

[15] The CMS Collaboration, "CMS: The TriDAS project. Technical design report: Data acquisition and high-level trigger," CERN-LHCC-2002-026

[16] W. Adam, B. Mangano, T. Speer and T. Todorov, "Track reconstruction in the CMS tracker," CERN-CMS-NOTE-2006-041

[17] I. Belotelov *et al.*, "Study of Drell-Yan Di-muon Production with the CMS Detector," CERN-CMS-NOTE in preparation.

[18] S. Abdullin *et al.*, "Sensitivity of the muon isolation cut efficiency to the underlying event uncertainties," CERN-CMS-NOTE-2006-033

APPENDIX A. Reconstruction of charged tracks

Charged track reconstruction relies on the Combinatorial Track Finder, which is described elsewhere [16]. Initial track segments (seeds) are searched for by combining two hits in the pixel layers, compatible with a helix originating from the beam spot area. The default algorithm allows to reconstruct tracks with p_T above $0.9\,$GeV/c. However, the same algorithm can be used in special conditions (with reduced thresholds for the seeds) achieving reasonable performances from $p_T = 0.5\,$GeV/c onwards. We will refer to these conditions as "standard" and "optimized", respectively.

In this analysis, general quality criteria are adopted for both "standard" and "optimized" charged track reconstruction, which require at least five hits. Between five and seven hits we also require absence of no consecutive hits. The χ^2 of the fit has to be such that $\chi^2/N_{dof} < 5$ and the maximum allowed longitudinal and transverse distance to the primary vertex of the leading interaction are set to $500\mu m$ and $1mm$, respectively.

In order to estimate the efficiencies and the amount of fakes in the two configurations, an association criteria is adopted which requires that at least 50% of the hits are shared between the reconstructed and the simulated track. The "standard" configuration figures are quoted on two jet samples which are generated using different ranges for the transverse momentum of the outgoing partons ($\hat{p}_T$). The results are reported in Figs. 24, 25, 26, and 27. In general, no sensitive dependency of these figures from the scale of the interaction is observed. Figures. 28, 29, 30, and 31 report the corresponding figures for the "optimized" configuration.
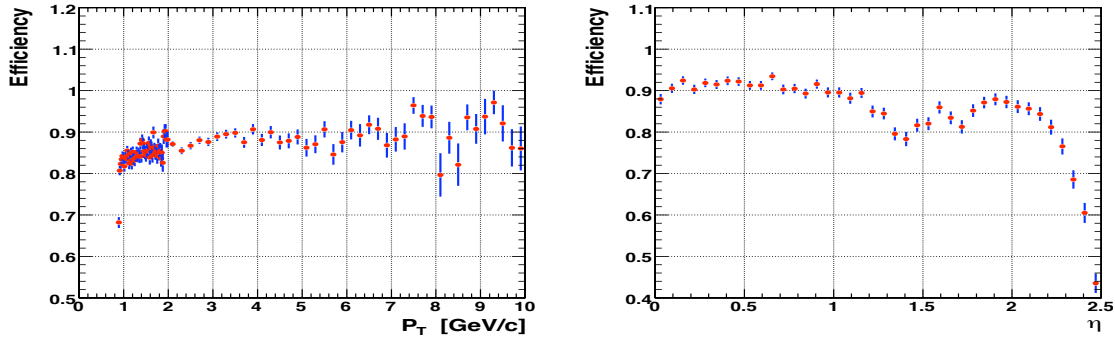

Figure 24: "Standard" charged track reconstruction in events with $30\,$GeV/c $< \hat{p}_T < 50\,$GeV/c. Efficiency versus p_T of charged tracks (*left*). Efficiency versus η of charged tracks (*right*).
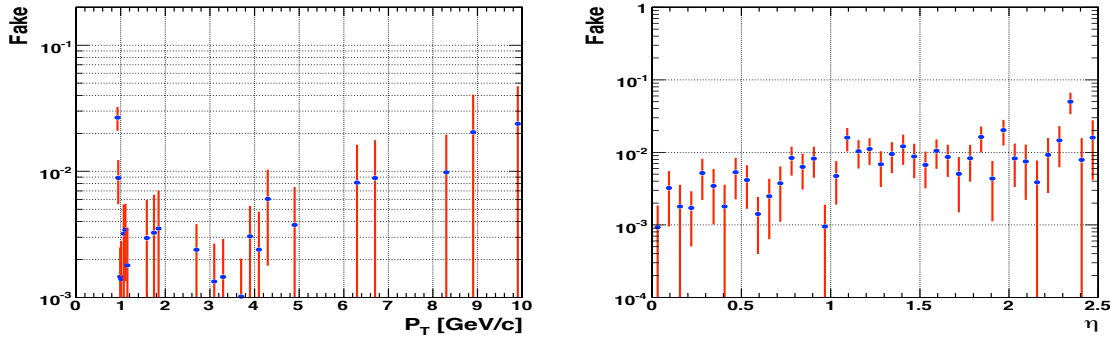

Figure 25: "Standard" charged track reconstruction in events with $30\,$GeV/c $< \hat{p}_T < 50\,$GeV/c. Fake rate versus p_T of charged tracks (*left*). Fake rate versus η of charged tracks (*right*).
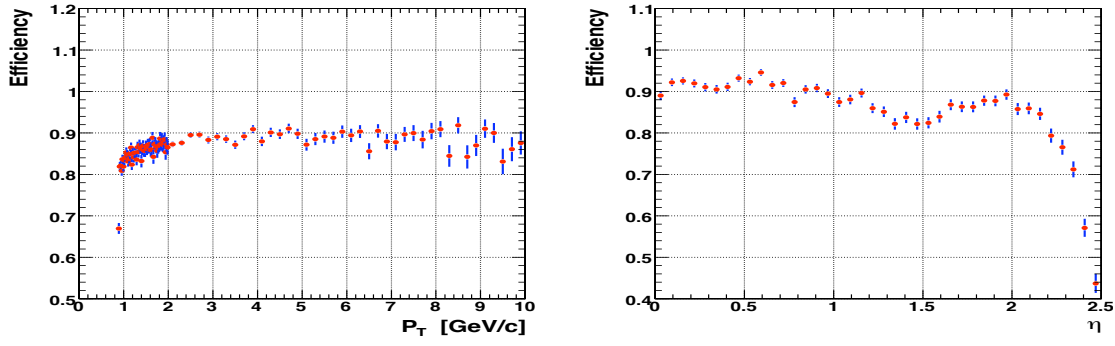
19

Figure 26: "Standard" charged track reconstruction in events with $70 \, \text{GeV/c} < \hat{p}_T < 90 \, \text{GeV/c}$. Efficiency versus p_T of charged tracks (*left*). Efficiency versus η of charged tracks (*right*).
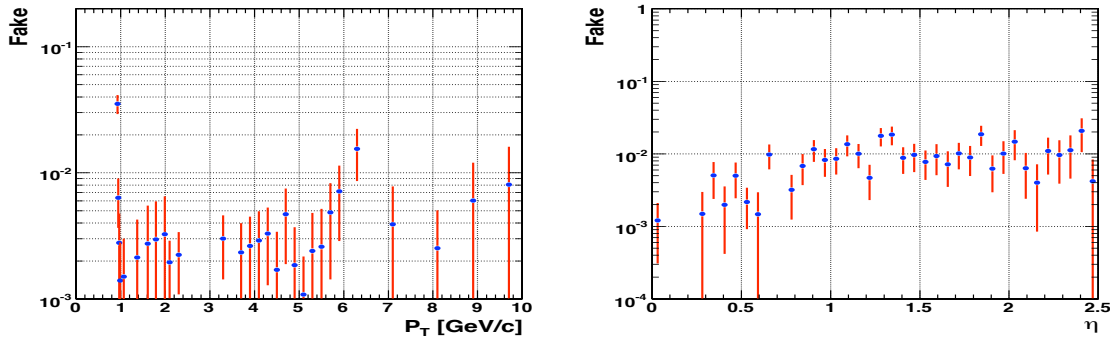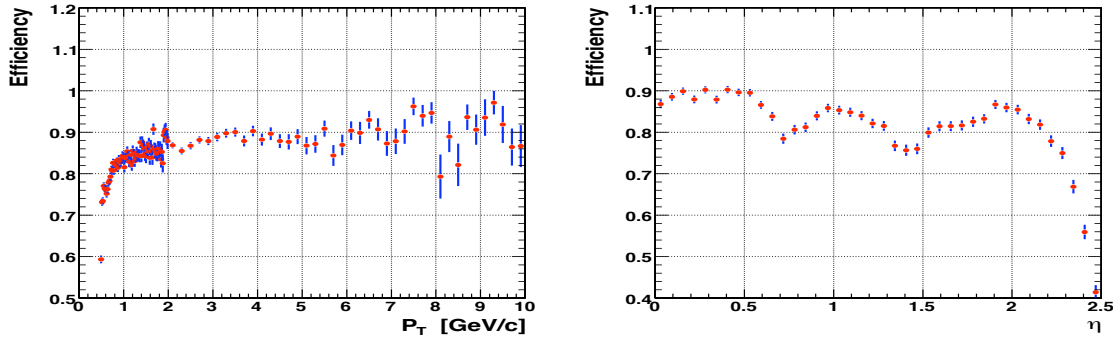

Figure 27: "Standard" charged track reconstruction in events with $70 \, \text{GeV/c} < \hat{p}_T < 90 \, \text{GeV/c}$. Fake rate versus p_T of charged tracks (*left*). Fake rate versus η of charged tracks (*right*).

Figure 28: "Optimized" charged track reconstruction in events with $30 \, \text{GeV/c} < \hat{p}_T < 50 \, \text{GeV/c}$. Efficiency versus p_T of charged tracks (*left*). Efficiency versus η of charged tracks (*right*).
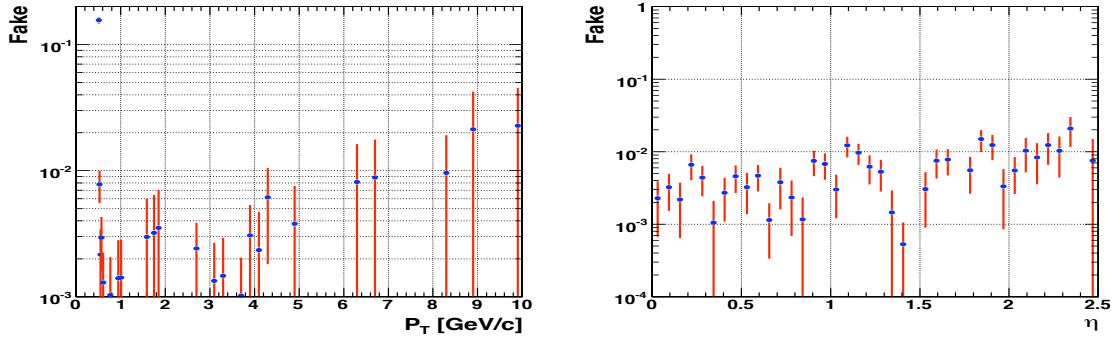
Figure 29: "Optimized" charged track reconstruction in events with $30\,\mathrm{GeV/c} < \hat{p}_T < 50\,\mathrm{GeV/c}$. Fake rate versus p_T of charged tracks (*left*). Fake rate versus η of charged tracks (*right*).
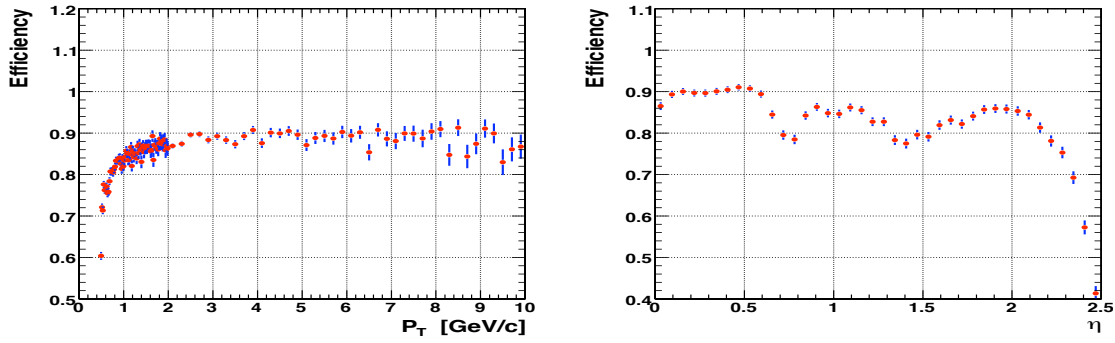

Figure 30: "Optimized" charged track reconstruction in events with $70\,\mathrm{GeV/c} < \hat{p}_T < 90\,\mathrm{GeV/c}$. Efficiency versus p_T of charged tracks (*left*). Efficiency versus η of charged tracks (*right*).
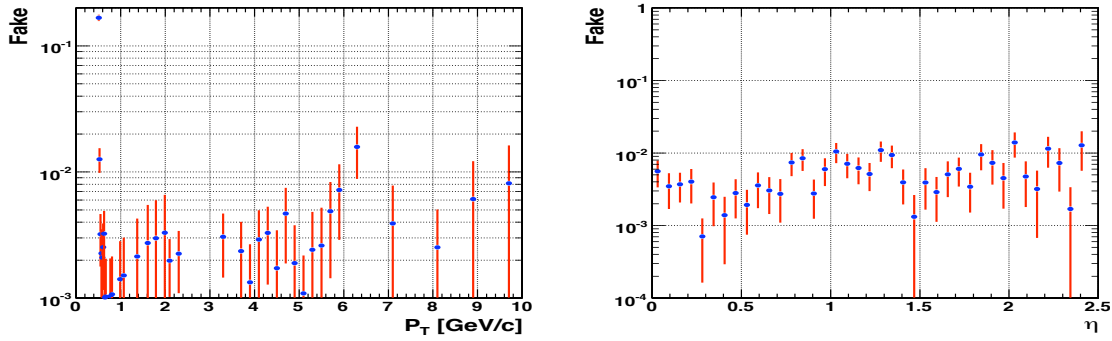

Figure 31: "Optimized" charged track reconstruction in events with $70\,\mathrm{GeV/c} < \hat{p}_T < 90\,\mathrm{GeV/c}$. Fake rate versus p_T of charged tracks (*left*). Fake rate versus η of charged tracks (*right*).

21